Supplementary Information (SI) for ChemComm.
This journal is © The Royal Society of Chemistry 2026

Metal-hydride-free one-pot synthesis of InSb/InP core/shell quantum dots for light-emitting diode

Cong Zhang[a,b], Hiroyuki Yamada[a], Daniel Limouchi[a,b], Kazuhiro Nemoto[*a] , Naoto Shirahata[*a,b,c].

Experimental Section

Reagents and Materials: Indium(III) acetate [$In(Ac)_3$, 99.99%, Aldrich], zinc acetate [$Zn(Ac)_2$, 99.99%, Aldrich], antimony(III) chloride [$SbCl_3$, 99.95%, Aldrich], zinc oxide [ZnO, 99.999%, Aldrich], lauric acid [LA, 98%, Tokyo Chemical Industry], palmitic acid (PA, 98%, Tokyo Chemical Industry), trioctylphosphine (TOP, 97%, Aldrich), tris(trimethylsilyl)-phosphine [$(TMS)_3P$, 98% Strem Chemicals], tris(dimethylamino)phosphine $P(NMe_2)_3$, 97%, Aldrich], 1-octadecene [ODE, 90%, Aldrich], oleylamine [OLA, 80-90%, Thermo Scientific Chemicals], 4,4′,4″-Tri-9-carbazolyltriphenylamine [TCTA, 99%, Tokyo Chemical Industry], were used without further purification. The purity of argon gas used for the synthesis was 99.999%.

Preparation of Sb precursor: $SbCl_3$ (0.09 mmol) was dissolved in OLA (2 mL) by stirring the mixture at 70 °C for overnight in an Ar-filled glove box that was continuously monitored to maintain both oxygen and water levels of $O_2 \leq 1$ ppm and $H_2O \leq 5$ ppm.
Preparation of $P(NMe_2)_3$-OLA: $P(NMe_2)_3$ (0.9 mmol) was dissolved in 1 mL of OLA at room temperature in a same glovebox.
Preparation of InP shell precursor: 0.06 mmol of $In(Ac)_3$ and LA (0.18 mmol) were mixed with 2.5 mL of ODE 20 mL glass bottle with overnight degassing of the mixture was performed under vacuum conditions at 120 ºC for 12 hours. Then cool down to room temperature, mixed with 0.24 mmol $P(NMe_2)_3$ and 0.5 mL OLA for 5 min.

Synthesis of InSb core QDs: 0.3mmol of $In(Ac)_3$, 0.15 mmol of $Zn(Ac)_2$ and 1.2 mmol LA were mixed with 12.8 mL of ODE in a 50 mL three-necked flask which was fixed to a Schlenk line with a reflux condenser. Using an oil rotary vacuum pump, the flask was degassed and purged with Ar gas five times under vacuum conditions below 60 Pa. Degassing of the mixture was performed under vacuum conditions at 120 ºC for 12 hours. After filled with Ar gas, the solution was heated to 190 ºC. $SbCl_3$ precursor was quickly injected into the flask while Ar flowed. After 2 min, the OLA-$P(NMe_2)_3$ solution was quickly injected into the flask, resulting in change in color of the solution from colorless to black in several seconds. The flask was further heated to 250ºC in 5 min. Then maintain at 250 ºC for 4 min. Finally, the flask was cooled down to room temperature by fan.

Synthesis of InSb/InP core/shell QDs: 0.3mmol of $In(Ac)_3$, 0.15 mmol of $Zn(Ac)_2$ and 1.2 mmol LA were mixed with 12.8 mL of ODE in a 50 mL three-necked flask which was fixed to a Schlenk line with a reflux condenser. Using an oil rotary vacuum pump, the flask was degassed and purged with Ar gas five times under vacuum conditions below

60 Pa. Degassing of the mixture was performed under vacuum conditions at 120 ºC for 12 hours. After filled with Ar gas, the solution was heated to 190 ºC. $SbCl_3$ precursor was quickly injected into the flask while Ar flowed. After 2 min, the OLA-$P(NMe_2)_3$ solution was quickly injected into the flask, resulting in change in color of the solution from colorless to black in several seconds. The flask was further heated to 250ºC in 5 min and maintain 250 ºC for 4 min. Then, inject InP shell precursor by dropwise and maintain 250 ºC for 6 min. Finally, the flask was cooled down to room temperature by fan.

Purification of QDs: As shown in Scheme 1. The as-synthesized solution was transferred to a centrifuge tube and centrifuged at 9000 rpm for 10 min. The precipitate and supernatant liquid were separated into respective centrifuge tubes. Acetone was added to the centrifuge tube until the supernatant became turbid and then centrifuged at 9000 rpm for 5 min. The supernatant was discarded. The precipitate was redispersed in 5 ml of hexane as crude QDs solution.

Separation of QDs-BC and QDs-SC: The crude QDs solution was subjected to a centrifugation process to separate QDs-BC and QDs-SC. Specifically, the crude QDs were centrifuged at 9000 rpm for 5 min after the addition of 3 mL of ethanol. The resulting precipitate was collected as QDs-BC. The supernatant was then further centrifuged at 9000 rpm for 5 min after adding an additional 2 mL of ethanol. The precipitate obtained from this step was designated as QDs-SC, while the colorless or pale-yellow supernatant was discarded. Collected QDs were washed with hexane and ethanol mixture (5 mL hexane and 5 mL ethanol for QDs-SC; 5 mL hexane and 3 mL ethanol for QDs-BC) for 3 times then dried by evacuation for 2 min, then stored in Ar atmosphere.

Synthesis of InP QDs for EXAFS: Refer to our previous work[1]. 0.45 mmol of $In(Ac)_3$, 0.075 mmol of $Zn(Ac)_2$ and PA (0.5 mmol) were mixed with 6.3 mL of ODE in a 50 ml three-necked flask which is fixed to a Schlenk line with a reflux condenser. Degassing of the mixture was performed at 120 °C for 12 h under vacuum conditions. The degree of vacuum was controlled at 30 Pa which was measured using a capacitance manometer (ULVAC, Japan). The flask was filled with argon and cooled down to room temperature. The $(TMS)_3P$-TOP was quickly injected into the flask in an argon flow, heated to 40 °C under vacuum and kept for 10 min for the evaporation of hexane. Then, the flask was refilled with argon, heated to 300 °C within 7.5 min and kept for 10 min. After then, the flask was cooled down to room temperature, and then acetone was added for centrifugation for 5 min at 10 000 rpm, the supernatant was decarded and InP QDs precipitate stored in argon-filled vials before EXAFS measurement.

Fabrication of QLED devices: A QD ink with a concentration of 10 mg/mL was prepared by dispersing 5 mg of QDs in 0.5 mL of toluene. Indium tin oxide (ITO)–coated soda-lime glass substrates (2 mm × 20 mm, 130 nm ITO thickness, sheet resistance 10–14 Ω/sq) were cleaned using a UV–ozone cleaner and subsequently transferred into an Ar-filled glovebox. A ZnO nanoparticle solution was first spin-coated onto the substrate at 1500 rpm for 30 s, followed by baking at 120 °C for 10 min. Then, the 10 mg/mL QD ink was spin-coated at 1500 rpm for 30 s and baked on a hot plate at 120 °C for 10 min. Finally, the substrates were transferred into a vacuum chamber for sequential deposition of 30 nm TCTA, 10 nm MoO_3, and 200 nm Al electrode (10 mm × 2 mm) layers. The ZnO film, serving as both the electron injection layer (EIL) and the electron transport layer (ETL), possesses a valence band which lies significantly below that of the QDs, effectively suppressing hole leakage from the emissive layer. In contrast, the MoO_3 film, functioning as both the hole injection layer (HIL) and the hole transport layer (HTL), provides a shallow work function that promotes efficient hole injection. The thermally evaporated TCTA film between the MoO_3 and QD layers further optimizes the energy-level alignment: its shallow HOMO level enables effective hole transport from MoO_3 to the QD layer, while its low LUMO level leads to suppressed electron leakage from the QDs to MoO_3. This energy-level configuration ensures balanced carrier injection and efficient radiative recombination within the emissive QD layer.

Observation and analysis of cross-sectional microstructures: Cross-sectional microstructures of the devices were examined by focused ion beam scanning electron microscopy (FIB-SEM) using a ZEISS Auriga laser (Carl Zeiss, Germany). A carbon protective layer was deposited prior to Ga^+ ion milling to prepare cross-sections, which were subsequently observed by high-resolution SEM at an accelerating voltage of 1 kV with a stage tilt angle of 54°.

Characterization: X-ray powder diffraction (XRD) patterns were measured on MiniFlex 600 (Rigaku, Japan). Transmission electron microscopic (TEM) and scan TEM (STEM) images were obtained from JEOL-JEM 2100 microscope, operating at 200 kV. Optical absorption and emission properties were measured with colloidal solution of the QDs. Optical absorption spectra were measured by a UV-vis spectrophotometer (JASCO V-650, Japan) with an integrated sphere. Photoluminescence (PL) and electroluminescence (EL) measurement was carried out using a modular double grating Czerny−Turner monochromator and an iHR 320 emission monochromator (1200 lines/mm of gratings) coupled to a photomultiplier tube (PMT) on a NanoLog Horiba Jovin Yvon

spectrofluorometer with a 450 W xenon arc lamp (EL measurement was without xenon lamp). The spectral resolution of the system is around 0.3 nm. To avoid scattered excitation lights, a cut filter for 395 nm-light was placed in front of the monochromator-PMT setup. The absolute PL quantum yields (QYs) were measured at room temperature using the QY measurement extended system C13534-01 from Hamamatsu Photonics Co., Ltd. with a 150 W xenon lamp coupled to a monochromator for wavelength discrimination, an integrating sphere as a sample chamber, and a multichannel analyzer for signal detection. Electrical and optical characterization of the devices was performed using a calibrated silicon photodetector (Hamamatsu Photonics, Japan) coupled with a Keithley 2635B and 2400 source meter.

Measurement of EXAFS: EXAFS measurements were conducted at the AR-NW10A beamline of the Photon Factory Advanced Ring (PF-AR, 6.5 GeV, 50 mA) at the High Energy Accelerator Research Organization (KEK), Tsukuba, Japan. A Si (311) double-crystal monochromator was used to monochromatize the incident X-ray beam. Indium K-edge EXAFS spectra were recorded in transmission mode. The energy scale was calibrated using a standard Indium foil. The XAFS spectra were processed using the ATHENA software in the Demeter package.

Calculation of EQE and optical power density: The external quantum efficiency (EQE) and optical power density were evaluated assuming Lambertian EL emission, a widely adopted approximation for bottom-emitting QLEDs without pronounced microcavity effects, where the angular EL intensity distribution closely follows Lambertian behaviour.[2-5] EQE is defined as the ratio of the number of photons emitted from the device to the number of injected electrons per unit time and was calculated using the following equation[6]:

$$EQE\ (\%) = \frac{N_p(V) \times |e| \times g}{I_d(V)} \times 100 \#Eq.1$$

where $N_p(V)$ is the number of photons detected by the photodiode, $|e|$ is the elementary charge, $I_d(V)$ is the device current at an applied voltage V, and g is the geometry factor accounting for the ratio between the total emitted photon flux and that collected by the photodiode. The geometry factor g is given by:

$$g = \frac{a^2 + L^2}{a^2} \#Eq.2$$

where a is the radius of the photodiode aperture and L is the distance between the emitting surface and the photodiode.[7] In this study, $a = 2.5\ mm$ and $L = 2.2\ mm$, yielding a

geometry factor of $g = 1.7744$. The photon number $N_p(V)$ was derived from the EL spectrum and the measured photodiode current I_p^m according to the following relation:

$$N_p(V) = \int_{\lambda_i}^{\lambda_f} EL(\lambda) \times \frac{I_p^m}{I_p^{'}(\lambda)} d\lambda \#Eq.3$$

Here, $I_p^{'}(\lambda)$ denotes the photocurrent generated by a unit photon flux and is calculated from Planck's constant h, the speed of light in vacuum c, the EL emission wavelength λ, and the spectral responsivity of the photodiode $R(\lambda)$:

$$I_p^{'}(\lambda) = \int_{\lambda_i}^{\lambda_f} EL(\lambda) \times \frac{hc}{\lambda} \times R(\lambda) d\lambda \#Eq.4$$

By evaluating $N_p(V)$ over the entire applied voltage range and substituting the resulting values into $Eq.1$, voltage-dependent EQE profiles were obtained. The optical power density $P(V)$ was calculated as follows:

$$P(V) = \int_{\lambda_i}^{\lambda_f} EL(\lambda) \times \frac{I_p^m}{I_p^{'}(\lambda)} \times \frac{hc}{\lambda} d\lambda \#Eq.5$$

The optical power density was obtained by normalizing the optical power to the emission area A:

$$Optical\ power\ density\ (W/cm^2) = \frac{P(V)}{A} \#Eq.6$$

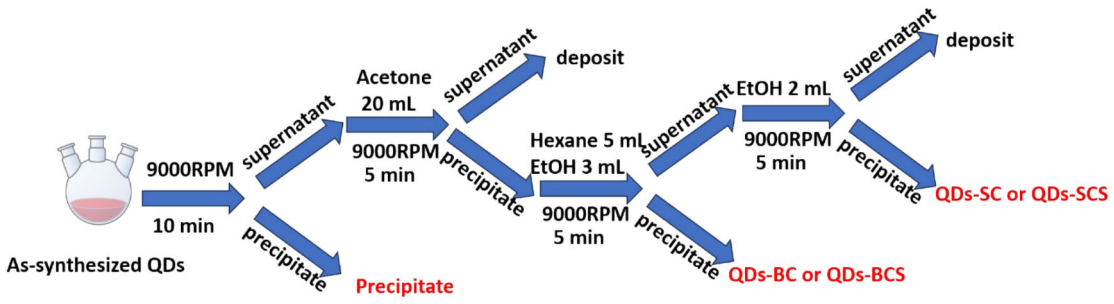

Scheme S1. The schematic illustration of the centrifugation process.

Note: The as-synthesized QDs were initially centrifuged to remove insoluble residues, leaving a QD-containing supernatant. The insoluble precipitate was bulk InSb. The supernatant was then treated with a large amount of anhydrous acetone to induce QDs precipitation. The obtained QDs precipitate was redispersed in 5 mL of hexane and subsequently subjected to stepwise centrifugation with gradually increasing volumes of ethanol to achieve separation by particle size and composition. Upon the addition of 3 mL of ethanol, centrifugation produced a precipitate (assigned as QDs-BC or QDs-BCS) and a supernatant. Further addition of 2 mL of ethanol to this supernatant followed by centrifugation yielded another precipitate (QDs-SC or QDs-SCS), leaving a colorless or yellow supernatant.

QDs	PLQY of InSb	PLQY of core/shell	Reference
InSb	almost nonemissive	none	8
InSb	almost nonemissive	none	9
InSb	0.2 %	none	10
InSb	0.5 %	none	11
InSb	2-3 %	none	12
InSb, InSb/InAs	not mentioned	not mentioned	13
InSb, InSb/InP	almost nonemissive	3.7 %	14
InSb, InSb/InP	almost nonemissive	10 %	15
InSb, InSb/InP	0.8 %	7 %	**This work**

Table S1. Table of PLQY in reported InSb QDs and InSb core/shell QDs.

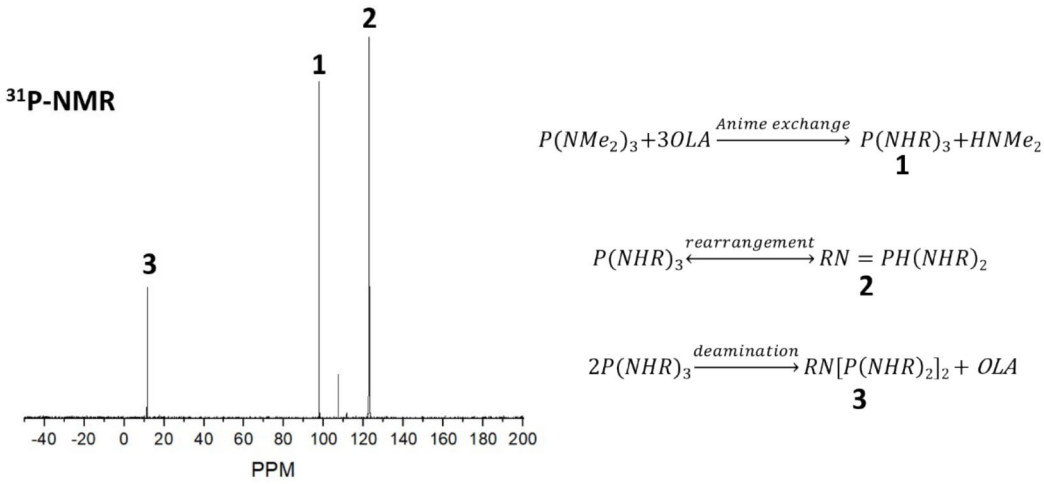

Figure S1. ^{31}P-NMR spectrum of the $P(NMe_2)_3$/OLA precursor. Formation of product **1** by amine exchange of $P(NMe_2)_3$ with OLA, formation of **2** by tautomerization equilibrium, and formation of bridging products **3** by deamination. The reactions refer to reference.[18]

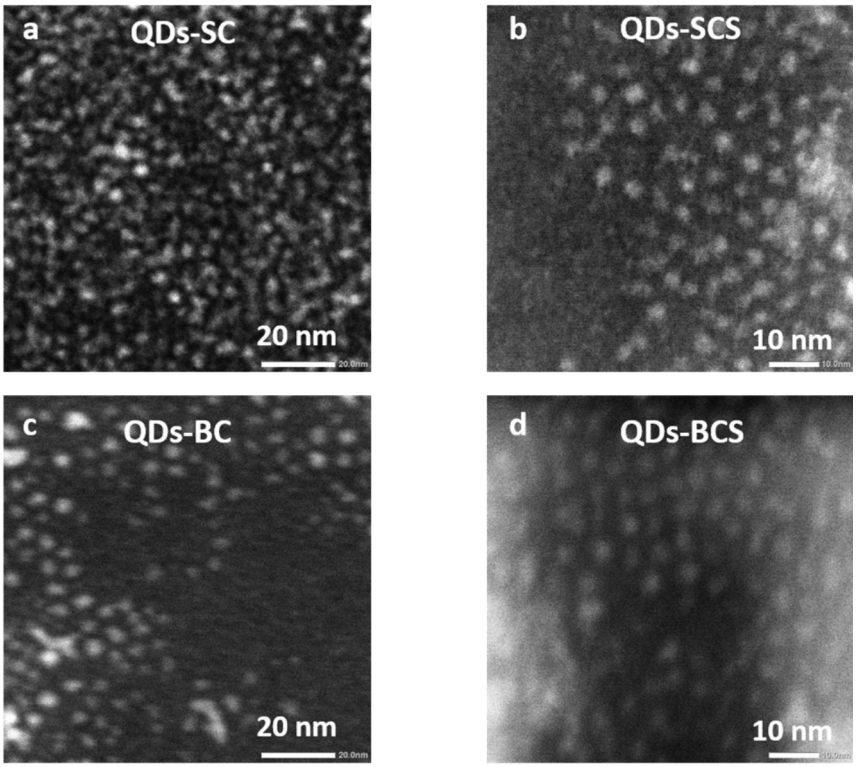

Figure S2. HAADF-STEM images of the QDs-SC (a), QDs-SCS (b), QDs-BC (c), QDs-BCS (d).

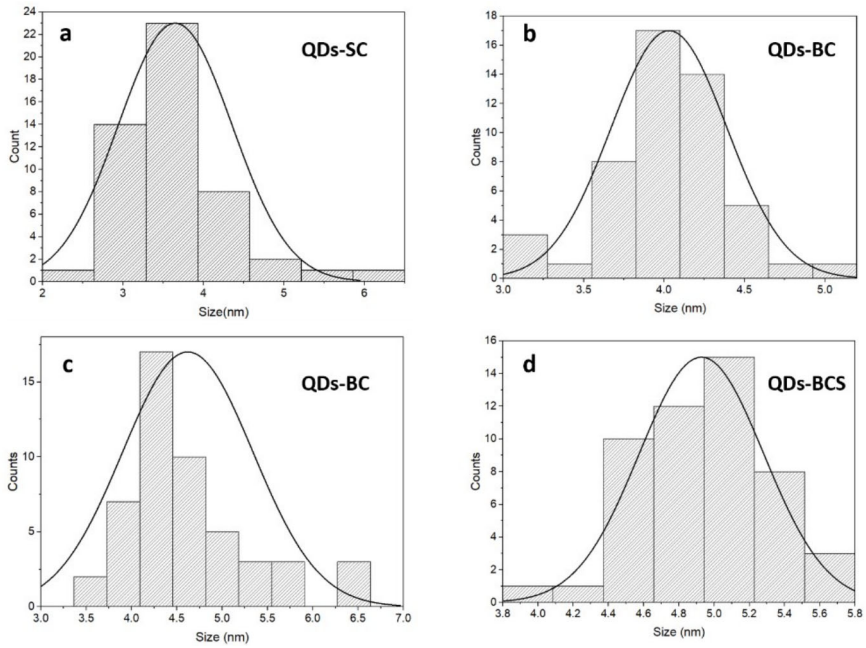

Figure S3. Size distribution profiles of the QDs-SC (**a**), QDs-SCS (**b**), QDs-BC (**c**), QDs-BCS (**d**). The particle size distribution was determined from the statistical analysis of the HAADF-STEM images.

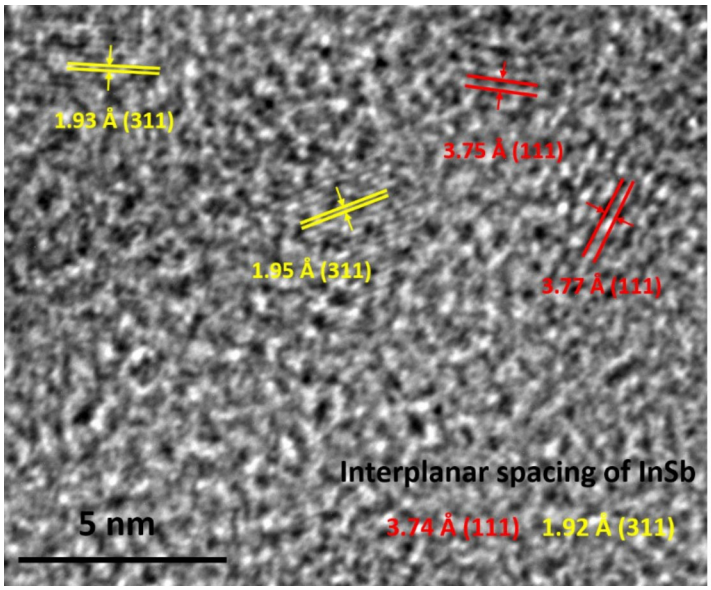

Figure S4. The HRTEM of QDs-SCS. Stripes distance close to InSb (111) and (311) facets, revealing the core of the QDs-SCS is InSb.

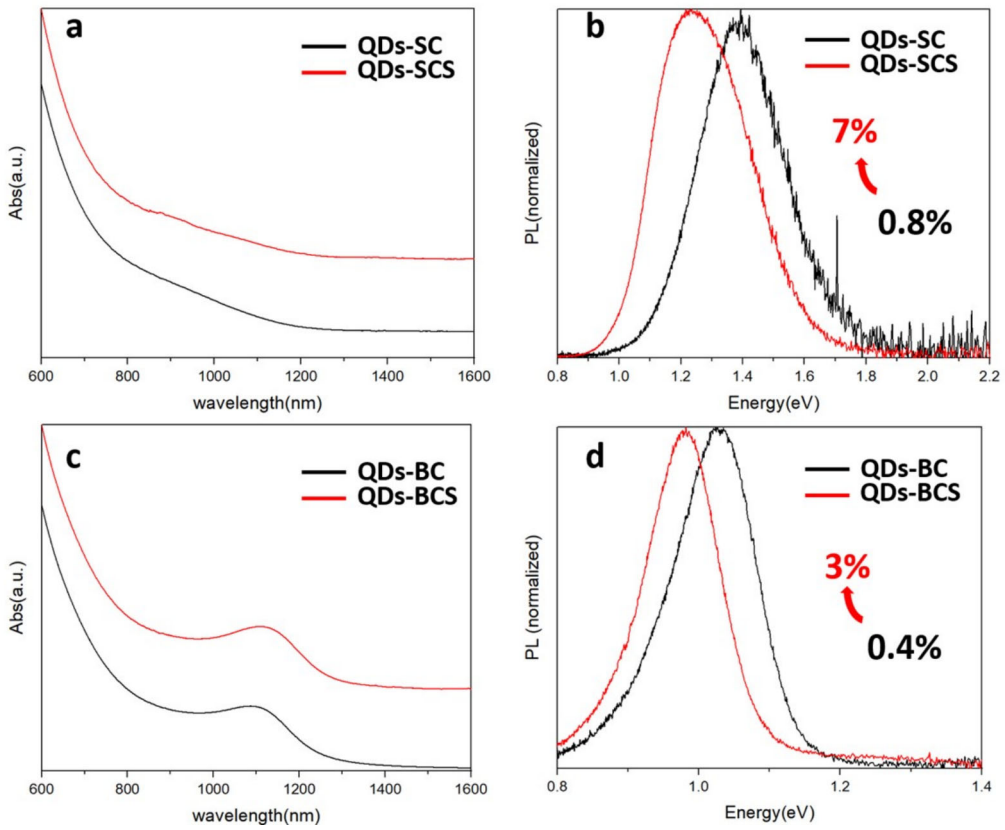

Figure S5. **a**) UV-VIS-NIR absorption spectra of the QDs-SC (black) and QDs-SCS (red); **b**) PL spectra of the QDs-SC (black) and QDs-SCS (red); **c**) UV-VIS-NIR absorption spectra of the QDs-BC (black) and QDs-BCS (red); **d**) PL spectra of the QDs-BC (black) and QDs-BCS (red).

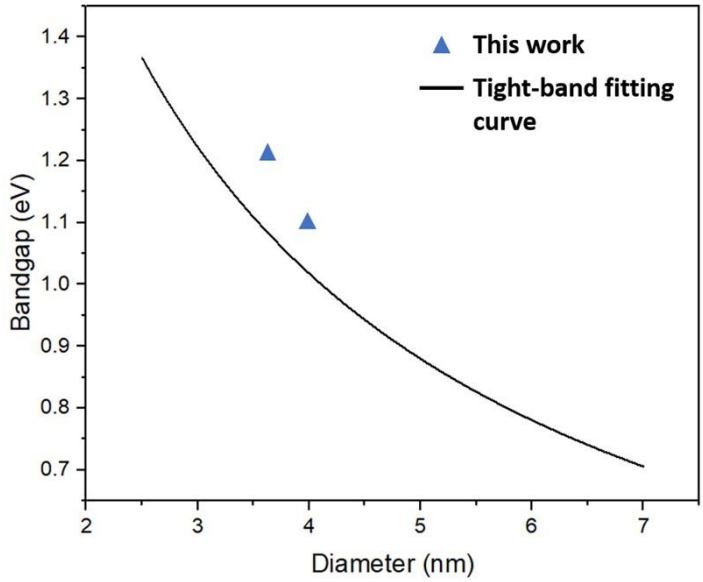

Figure S6 The correlation between the energy bandgap and particle size of the synthesized InSb QDs in this work, together with the tight-band model curve. The blue triangles are our data: QDs-BC (4.0 nm, 1.13 eV) and QDs-SC (3.6 nm, 1.3 eV)

Note: tight-band curve is generated by equation[16]:

$$Eg(d) = 0.17 + \frac{1}{0.2295d + 0.2618}$$

In which E_g is the bandgap of InSb QDs and d is the diameter of InSb QDs.

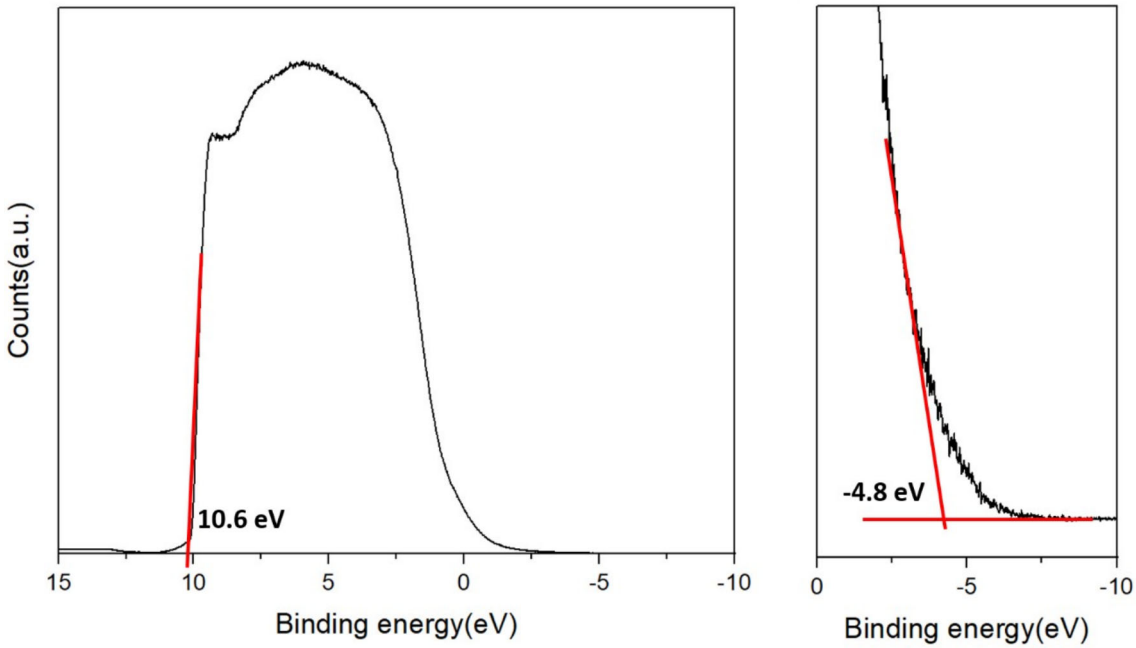

Figure S7 The high (left) and low (right) binding energy cutoff regions' UPS spectra of InSb QD film coated on ITO.

Note: The work function is generally calculated by the difference in energy between the secondary electron cutoff and the excitation photon energy (hv = 21.22 eV). For the InSb QD thin film, the low and high binding energy cutoff regions of the UPS spectra are -4.8 eV (c_{onset}) and 10.6 eV ($cutoff_{high}$), respectively. The HOMO (e_v) value was calculated to be 5.82 eV from the following equations:[17]

$$e_v = hv - (cutoff_{high} - c_{onset})$$

Using the magnitude of bandgap of the QD-SCS (1.30 eV), which determined by UV-Vis-NIR absorption, the LUMO (e_c) was calculated to be 4.52 eV (QDs-SCS device).

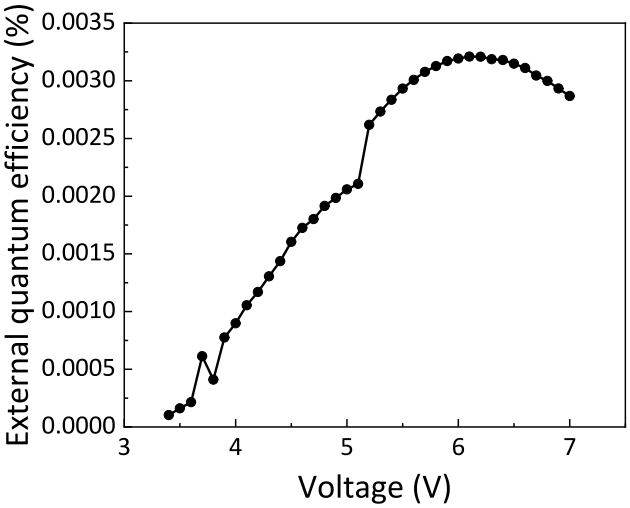

Figure S8. EQE-voltage curve of LED device.

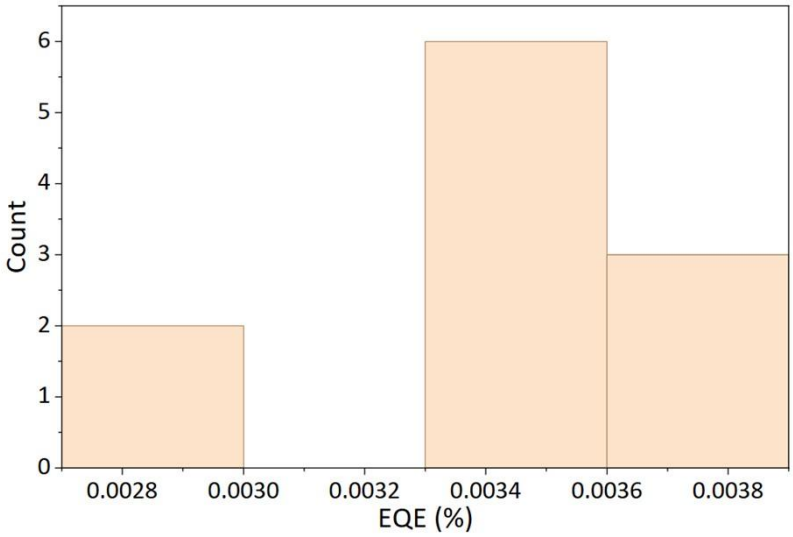

Figure S9. EQE reproducibility of LED devices.

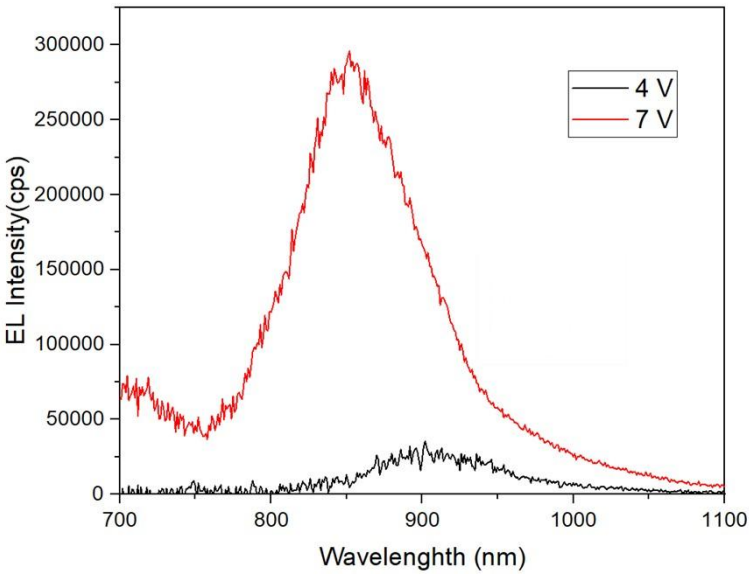

Figure S10. EL spectra of the QDs-SCS-based QLED device operated at 4 V (black) and 7 V (red).

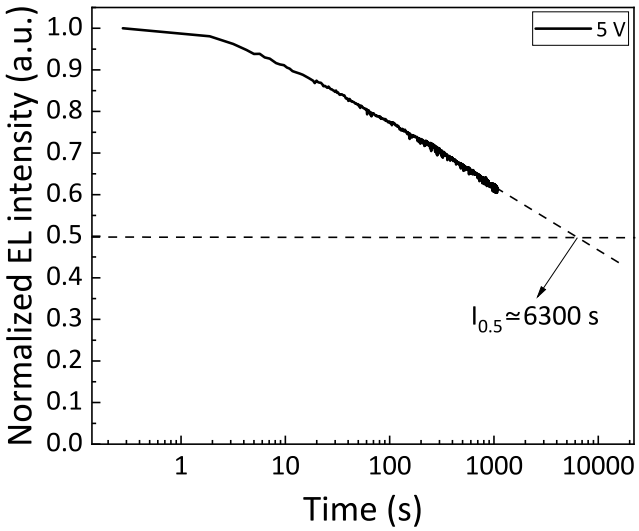

Figure S11. Ambient stability of LED device. work at 5 V. Half-lifetime ~ 6300s.

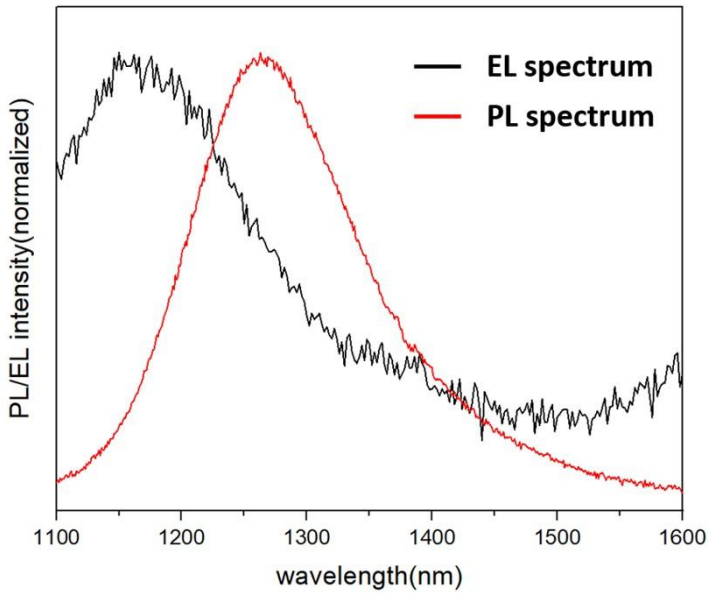

Figure S12. EL spectrum (black) of the QDs-BCS-based QLED device work at 10 V and PL spectrum (red) of the corresponding QDs-BCS.

Reference:

1. K. Nemoto, J. Watanabe, H. T. Sun, N. Shirahata, Nanoscale, 2022, **14**, 9900-9909.
2. Greenham, N. C.; Friend, R. H.; Bradley, D. D. C. Angular Dependence of the Emission from a Conjugated Polymer Light-Emitting Diode: Implications for Efficiency Calculations. Advanced Materials 1994, 6 (6), 491–494. https://doi.org/10.1002/adma.19940060612.
3. Jin, W.; Deng, Y.; Guo, B.; Lian, Y.; Zhao, B.; Di, D.; Sun, X.; Wang, K.; Chen, S.; Yang, Y.; Cao, W.; Chen, S.; Ji, W.; Yang, X.; Gao, Y.; Wang, S.; Shen, H.; Zhao, J.; Qian, L.; Li, F.; Jin, Y. On the Accurate Characterization of Quantum-Dot Light-Emitting Diodes for Display Applications. npj Flexible Electronics 2022, 6 (1), 35. https://doi.org/10.1038/s41528-022-00169-5.
4. Dai, X.; Zhang, Z.; Jin, Y.; Niu, Y.; Cao, H.; Liang, X.; Chen, L.; Wang, J.; Peng, X. Solution-Processed, High-Performance Light-Emitting Diodes Based on Quantum Dots. Nature 2014, 515 (7525), 96–99. https://doi.org/10.1038/nature13829.
5. Shen, H.; Gao, Q.; Zhang, Y.; Lin, Y.; Lin, Q.; Li, Z.; Chen, L.; Zeng, Z.; Li, X.; Jia, Y.; Wang, S.; Du, Z.; Li, L. S.; Zhang, Z. Visible Quantum Dot Light-Emitting Diodes with Simultaneous High Brightness and Efficiency. Nat Photonics 2019, 13 (3), 192–197. https://doi.org/10.1038/s41566-019-0364-z.
6. Supran, G. J. S. Enhancing Quantum-Dot Luminescence in Visible and Infrared Light Emitting Devices. Ph.D. Thesis, Massachusetts Institute of Technology, Cambridge, MA, USA 2016.
7. Yamada, H.; Nagao, T.; Shirahata, N. Rational Impurity Doping for Enhanced Hole Mobility in Silicon Quantum Dots for Light-Emitting Diodes. Nanoscale Adv 2025. https://doi.org/10.1039/D5NA00349K.
8. S. Chatterjee, K. Nemoto, B. Ghosh, H.-T. Sun, N. Shirahata, ACS Appl. Nano Mater., 2023, 6, 15540–15550.
9. S. Chatterjee, K. Nemoto, H.-T. Sun and N. Shirahata, Nanoscale Horizons, 2024, 9, 817-827.
10. C. Z. Kazuhiro Nemoto, Hong-Tao Sun, and Naoto Shirahata, ChemRxiv, 2025, DOI: 10.26434/chemrxiv-2025-x9c2k.
11. Muhammad, D. Choi, D. H. Parmar, B. Rehl, Y. Zhang, O. Atan, G. Kim, P. Xia, J. M. Pina, M. Li, Y. Liu, O. Voznyy, S. Hoogland and E. H. Sargent, Advanced Materials, 2023, 35, 2306147.
12. Y. Zhang, P. Xia, B. Rehl, D. H. Parmar, D. Choi, M. Imran, Y. Chen, Y. Liu, M. Vafaie, C. Li, O. Atan, J. M. Pina, W. Paritmongkol, L. Levina, O. Voznyy, S. Hoogland and E. H. Sargent, Angewandte Chemie International Edition, 2024, 63,

e202316733.
13. H. Seo, H. J. Eun, A. Y. Lee, H. K. Lee, J. H. Kim and S.-W. Kim, Advanced Science, 2024, 11, 2306439.
14. L. Peng, Y. Wang, Y. Ren, Z. Wang, P. Cao and G. Konstantatos, ACS Nano, 2024, 18, 5113-5121.
15. L. Peng, Y. Wang, C. Rodà, A. Malla, M. Dosil, D. Mandal and G. Konstantatos, Advanced Science, 2025, 12, 2502775.
16. S. Busatto, M. de Ruiter, J. T. B. H. Jastrzebski, W. Albrecht, V. Pinchetti, S. Brovelli, S. Bals, M.-E. Moret, C. de Mello Donega, ACS Nano, 2020, **14**, 13146–13160.
17. P. R. Brown, D. Kim, R. R. Lunt, N. Zhao, M. G. Bawendi, J. C. Grossman, V. Bulovic, ACS Nano, 2014, **8**, 5863-5872.
18. A. Buffard, S. Dreyfuss, B. Nadal, H. Heuclin, X. Xu, G. Patriarche, N. Mézailles and B. Dubertret, *Chemistry of Materials*, 2016, **28**, 5925-5934.